ATMOSPHERIC SCIENCE

European supercell thunderstorms—A prevalent current threat and an increasing future hazard

Monika Feldmann[1]*†, Michael Blanc[2]†, Killian P. Brennan[2], Iris Thurnherr[2], Patricio Velasquez[2], Olivia Martius[1], Christoph Schär[2]

Supercell thunderstorms are the most hazardous thunderstorm category and particularly impactful to society. Their monitoring is challenging and often confined to the radar networks of single countries. By exploiting kilometer-scale climate simulations, we have derived a previously unknown characterization of supercell occurrence in Europe for the current and a warmer climate. The current climate shows several hundred supercells per convective season. Occurrence peaks are colocated with complex topography, e.g., the Alps. The absolute frequency maximum lies along the southern Alps and minima over the oceans and flat areas. Comparing a current-climate simulation with a pseudo–global warming +3°C global warming scenario, the future climate simulation shows an average increase of supercell occurrence by 11%. However, there is a spatial dipole of change with strong increases in supercell frequencies in central and eastern Europe and a decrease in frequency over the Iberian Peninsula and southwestern France.

INTRODUCTION

Supercell thunderstorms are among the most dangerous weather phenomena, responsible for severe wind gusts, large hail, torrential rain, and tornadoes (*1*). Severe convective storms, including supercells, have resulted in increasing insurance loss claims in recent years and were the costliest natural hazard in 2023 (*2*, *3*). These damage trends highlight the relevance of understanding the overall occurrence and changing behavior of supercells in a warming climate (*3*). While the observational record of supercell phenomena in the United States is starting to be sufficiently long to study trends (*4*, *5*), supercell monitoring in Europe is fragmented by country (*6*–*8*), and no long-term homogeneous record exists.

Previous observational work in Europe has focused on single countries or relied on using relatively coarse-grained proxy analyses (*6*, *7*, *9*). Most studies on severe convection in Europe focus on convective hazards, such as hail and lightning, rather than supercell thunderstorms explicitly (*10*–*13*). Analyses of proxy environments, usually consisting of instability and wind shear, often fail to capture the effects of complex terrain (*14*–*18*) and assume a stationarity of the proxy criteria and storm generation efficiency in a changing climate. Neither of these assumptions has been robustly assessed in a climate change context.

Using kilometer-scale simulations has enabled us to adequately simulate hourly (as opposed to daily) heavy precipitation events (*19*–*23*), and recent work suggests that these models successfully simulate hail (*24*), indicating good performance for deep moist convection. These studies also show an increase in heavy hourly and subhourly precipitation intensity with climate change, warranting a deeper investigation for supercells.

We aim to address the lack of homogeneous, high-quality supercell data by using a regional climate model. We use a kilometer-scale, 11-year, current-climate simulation over the European domain, which explicitly resolves supercell thunderstorms (*25*). The high resolution of our simulation allows most terrain effects to be captured, and the explicit resolution of the storm scale removes the necessity to rely on proxies. By tracking resolved supercells, we obtain a homogeneous frequency map of supercell occurrence in Europe. We use the frequency assessments of single countries to qualitatively validate the frequency map obtained through the model analysis. By perturbing the initial and lateral boundary conditions of the simulation to reflect a 3°C global warming level (GWL) derived from a general circulation model (GCM), an 11-year pseudo–global warming (PGW) simulation is produced (*26*, *27*), allowing us to analyze spatiotemporal frequency changes in supercell occurrence owed to climate change. A similar approach was pursued in the United States with promising results, albeit with coarser spatio-temporal resolution (*28*). Given the importance of the European mountain regions for convection, a higher resolution is necessary to resolve important topographical features (*29*).

RESULTS

Case-based model validation

The current-day 11-year-long climate simulation run with the regional climate model COSMO at 2.2-km horizontal resolution is driven by ERA-5 data (*30*) at the lateral boundaries. In the domain center, this results in relatively weak circulation and thermodynamic constraints through boundary forcing, which are similar to a multiday forecast rather than a high-resolution reanalysis (*27*, *31*). In addition, considering that we are dealing with an 11-year-long continuous climate run (rather than an initialized case study simulation), we expect considerable predictability limitations driven by the chaotic nature of the underlying thunderstorm dynamics. To validate the simulation's capability to produce supercell thunderstorms, we inspect the overall supercell activity on days with known outbreaks and compare the diurnal and seasonal cycles using the Swiss, radar-based supercell climatology (*32*). The model setup is designed to produce a representative climatology but not to reproduce individual thunderstorms. We therefore show a qualitative validation rather than a score-based verification. Further validation of the spatial distribution of current climatology is discussed in the

[1]Institute of Geography - Oeschger Centre for Climate Change Research, University of Bern, Bern, Switzerland. [2]Institute of Atmospheric and Climate Science, ETH Zürich, Switzerland.
*Corresponding author. Email: monika.feldmann@unibe.ch
†These authors contributed equally to this work.

"Occurrence of supercell thunderstorms in the current climate" section. We focus on 1 August 2017 (*7*) and 28 June 2021 (*33*), both days with prominent, long-track supercells occurring within the Swiss radar domain (Fig. 1). The simulated tracks are derived from the 5-min precipitation field and classified as supercells based on hourly three-dimensional (3D) vorticity and updraft data (see the "Supercell tracking" section in Materials and Methods). The observed supercells are tracked in radar reflectivity and classified in Doppler velocity every 5 min (see the "Observational reference" section in Materials and Methods).

In both cases, the simulation produces supercells, whose locations and track directions are similar to observed tracks. The different frequencies of detected rotation (dark gray dots) stem from the differing temporal resolution of rotation data. While the number of storms differs between model and observations, the agreement is encouraging given the expected limitations in mesoscale predictability. The observations are limited to the Swiss radar network, while the simulated tracks extend further into the neighboring countries. The model is indeed capable of producing long thunderstorm tracks with consistent rotation in complex terrain. Given the high occurrence of severe convection in the vicinity of substantial terrain in Europe (*11*, *12*), this is imperative to obtaining a representative supercell distribution.

The diurnal and seasonal cycles are depicted as empirical probability density functions, where the area under the curve integrates to 1, resulting in density values scaling inversely with the range of the *x* axis. In the model, the diurnal cycle of supercell activity peaks 2 hours before the observed cycle and has a sharper peak. This is a known bias of the COSMO model, also reflected in heavy precipitation (*25*). The seasonal cycle is reproduced very well, closely matching the radar observations.

Additional cases are included in the "Validation—Additional cases" section in the Supplementary Materials, where we analyze outbreaks across Europe based on severe storm reports (*34*) and severe weather outlooks (*35*). These contain both left- and right-moving modeled supercells. While some outbreak days are not reflected in the model, the majority of investigated outbreaks are successfully reproduced. Likewise, a few instances without reported severe convection trigger supercells in the model. These differences are likely driven by the uncertainties surrounding convective initiation (CI) and supercell reporting. Overall, the model produces ~60% fewer supercell tracks in Switzerland than are identified in radar data. A reduced sampling is expected, as a 2.2-km horizontal resolution will fail to resolve smaller and weaker mesocyclones. Likewise, the hourly resolution of the model tracking is bound to miss shorter or fluctuating storms. When filtering the radar dataset to mesocyclones crossing the full hour (98%

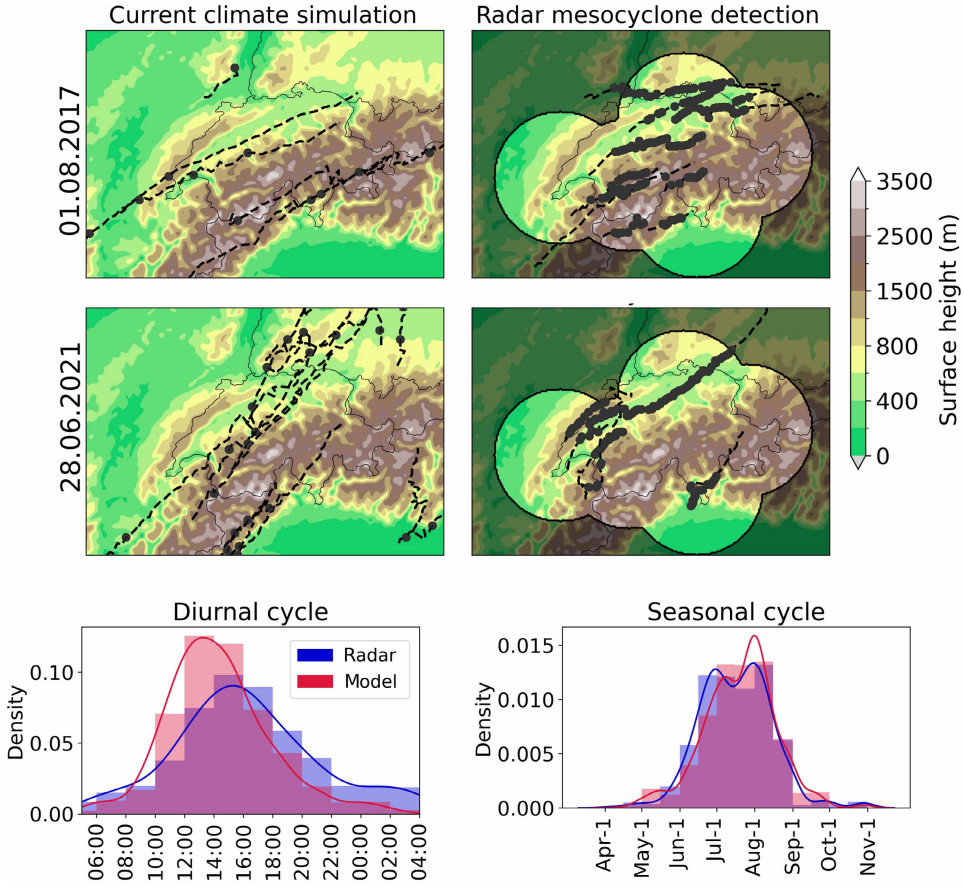

Fig. 1. Case validation of model with observations showing similar activity of supercells in Alpine regions on the same day. (**Top row**) 1 August 2017. (**Middle row**) 28 June 2021. (Left column) Supercells tracked in current climate simulation. (Right column) Radar-based mesocyclone detection. Precipitation-derived tracks are depicted in black dashed lines (5 min), identified rotation in dark gray dots (radar, 5 min; model, hourly), and the 100-km extent of the radar network in black contour. (**Bottom row**) Comparison of diurnal and seasonal cycles in the Alpine region obtained from radar and model data. For case study location, see Fig. 2A, Alps region.

of tracks) and mesocyclones with at least 5 km in diameter (40% of tracks), the number of detected mesocyclones within the radar-available time period 2016–2021 is virtually identical (model: 208, radar: 213). The model hence produces supercellular activity on the correct days and in the appropriate region, with a frequency reflecting the information scale of model data. We therefore conclude that the overall qualitative supercell activity in the model is comparable to confirmed cases, although skewed toward larger mesocyclones.

Occurrence of supercell thunderstorms in the current climate

We derive the annual average supercell frequency from the tracked supercells of the reanalysis-driven (ERA-5) current-climate simulation from 2011 to 2021 (see the "European climate simulations" section in Materials and Methods) (*30*). Figure 2A introduces the model domain and elevation map and the regions used for subsequent analyses. We focus on the area within the dashed black box for all further analyses.

The supercell frequency map in Fig. 2B uses a five grid point radius to grid each storm detection. Frequency clusters occur around major terrain features, such as the Pyrenees, Massif Central, Alps, and Dinaric Alps, revealing similar spatial patterns to observed hailstorm frequency in radar and satellite data and severe storm reports (*11*, *12*, *25*, *36*). The link between supercells and orography is supported by studies showing topography facilitating supercell development and intensification by locally increasing low-level shear and moisture (*18*, *37*, *38*).

On a regional scale, the distribution matches local climatologies. For example, in Switzerland, the frequency maxima in the Northern and Southern Prealps are successfully simulated (*7*, *32*). Germany's north-to-south frequency gradient is also present (*6*, *39*) as well as the elevated convective activity in the Massif Central in France (*11*, *12*) and the severe convective hot spot of eastern Spain (*40*–*43*). While we lack a local observation-based supercell climatology of the peak region in the Friulian Alps, this area is well-known for being Europe's most active tornado and severe hail storm region (*10*, *37*, *44*, *45*).

With local observation-based climatologies supporting the derived frequency map, this modeling approach allows us to obtain an overall supercell frequency map over Europe.

The seasonal cycle of supercell occurrence shows a meridional gradient (Fig. 2C). To smooth small-scale patterns, a 25 grid point storm radius is used in Fig. 2C, and areas with small sample sizes of <10 supercells during the 11 years are hatched. This reveals a clear meridional gradient, with supercells occurring primarily in summer over continental Europe and in fall in the Mediterranean. Because of a lack of extratropical storm triggers in summer, low-pressure systems only start reaching the Mediterranean again in fall, contributing to convective activity (*46*). A notable exception is Spain, which also peaks in mid-summer. Supercells largely track from southwest (SW) to northeast (NE) (*7*, *47*); hence, cells developing over the

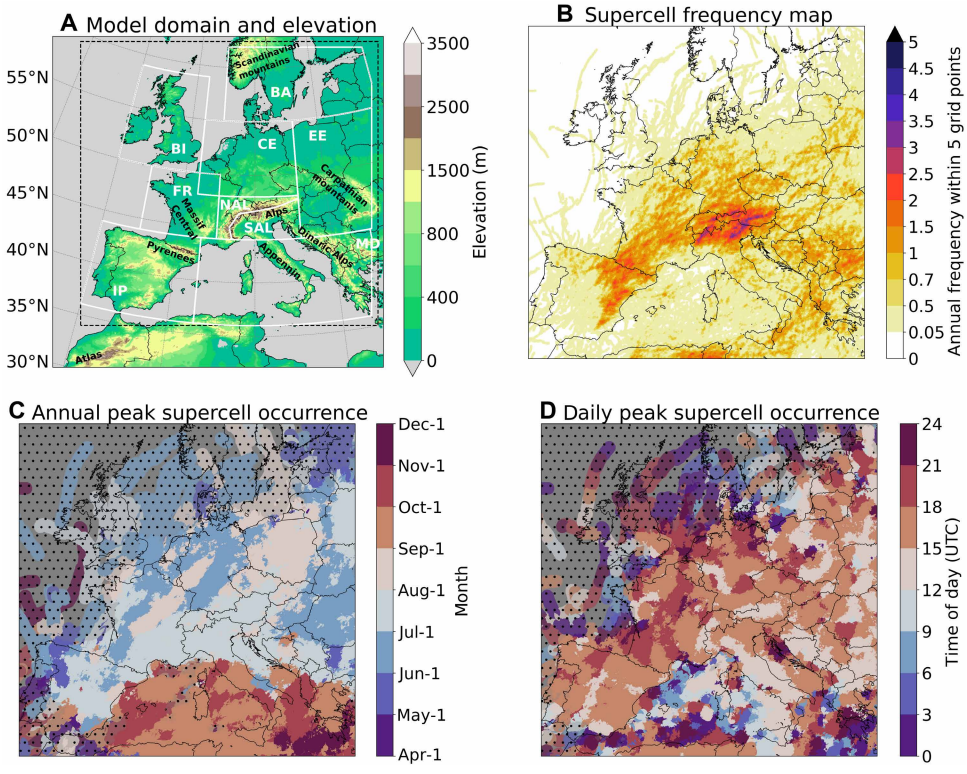

Fig. 2. Topography and 11-year supercell thunderstorm climatology from the current-day simulation showing supercell hotspots surrounding mountain ranges. (**A**) Topographic map of the domain showing analyzed domain (black dashed box), analysis regions (white boxes, for abbreviations, see Table 1), and mountain ranges (labeled in black). (**B**) Annual average supercell frequency 2011–2021, within five grid points. (**C**) Most active month of year, within 25 grid points, stippling covers areas with less than 10 supercells within 25 grid points and (**D**) most active time of day, within 25 grid points, 3-hourly smoothing, and stippling covers areas with less than 10 supercells within 25 grid points.

Mediterranean Sea in autumn do not affect the eastern part of the Iberian Peninsula.

Peak diurnal occurrence falls into the late afternoon hours with a zonal gradient, as shown in Fig. 2D. The peak hour in the day (universal time coordinated) for supercell activity is derived with a 25 grid point storm radius and 3-hourly smoothing. Given the longitudinal breadth, this corresponds to different local times throughout the domain with later peaks in France and earlier peaks in eastern Europe. Only the maritime areas, where activity is generally much lower, show peaks in the morning. Combined with peaking late in the season, this shows a preferred storm occurrence when the sea surface is still warm and the air above is relatively cool, leading to greater instability.

Topography plays an important role in the frequency distribution of supercell thunderstorms in Europe. A variety of mechanisms affect the prestorm environment and CI processes, contributing to high supercell frequencies (*48*). First, orographic flow modulation, affecting the local shear profile through flow channeling and directional forcing of surface flow, is one factor (*16*, *18*, *38*, *49*). This locally increases the magnitude of bulk shear and imposes directional shear. Especially inflow channeling increases storm relative helicity through increased inflow speed, which aligns with horizontal vorticity (*18*). Second, instability can be locally increased due to moisture advection, accumulation, and land moisture availability, where topography prevents moisture from being dispersed (*18*, *49*, *50*). In valleys, local moisture sources, such as lakes, provide a continuous moisture supply that is locally contained by the topography. Inflow channeling, particularly over the lake, increases the amount of moisture effectively retained by the storm, increasing instability in the inflow area (*18*). Third, topography also plays an important role in the development of elevated mixed layers: dry, stable layers in the lower atmosphere that delay CI and allow greater instability to build (*51*, *52*). This effect is more important at larger spatial scales in Europe, mostly analyzed with the "Spanish plume," where topography on the Iberian Peninsula is related to elevated mixed layers in France and the United Kingdom (*51*). Last, topography also plays an important role in lee-cyclogenesis, downstream of the mountain ranges (*53*, *54*), which contributes to convection, favoring environments and upscale growth toward mesoscale convective systems, as Rasmussen and Houze (*53*) show for Argentina.

The first two effects act more locally, on the meso-γ scale, whereas the last two have a spatially larger influence, on the meso-β to meso-α scale. While the frequency map of supercell thunderstorms in Europe shows elevated occurrence of supercells near topography, we further discuss the implications of modified environmental parameters in the "Changes in convective environments" section.

Occurrence of supercell thunderstorms at +3°C GWL

The future climate simulation is driven by the climate change Δ of a GCM at a GWL of +3°C compared to the preindustrial period using the PGW methodology (see the "European climate simulations" section in Materials and Methods), providing the data for a supercell frequency map for a future climate scenario in Fig. 3.

Figure 3A shows the difference in annual track number between the future and current climate simulations, with Fig. 3B showing the future climate supercell frequency map. Because of the small number of tracks per grid point, significance testing is performed in regional aggregations (as defined in Fig. 2A) with a Wilcoxon signed-rank test at $P \leq 0.05$ level. Significant increases are marked in solid lines and red shading, decreases in dashed lines and blue shading, and nonsignificant changes with dotted lines and gray shading (see inset in Fig. 3A). The overall track number increases significantly by 11%, and the activity shifts toward the northeast. The previous overall hot spot of the Alpine region emerges as an even stronger maximum than before, with the largest absolute increase in track number ($\geq$1 year^{-1}). The peak supercell frequency now exceeds four supercells within five grid points per year in the Austrian Alps. Pronounced increases also occur over southern Germany, eastern Europe, and northeastern Europe. In contrast, over the Iberian Peninsula and southern France, supercell frequency decreases. Table 1 shows the annual number of supercell tracks initiating in each region and the fraction of right-moving storms in the current and future climate simulation, as well as the relative change. A Wilcoxon signed-rank test is used to establish statistically significant changes at the $P \leq 0.05$ level. The largest relative change occurs in the Baltic, with a 110% increase from the current climate. Significant

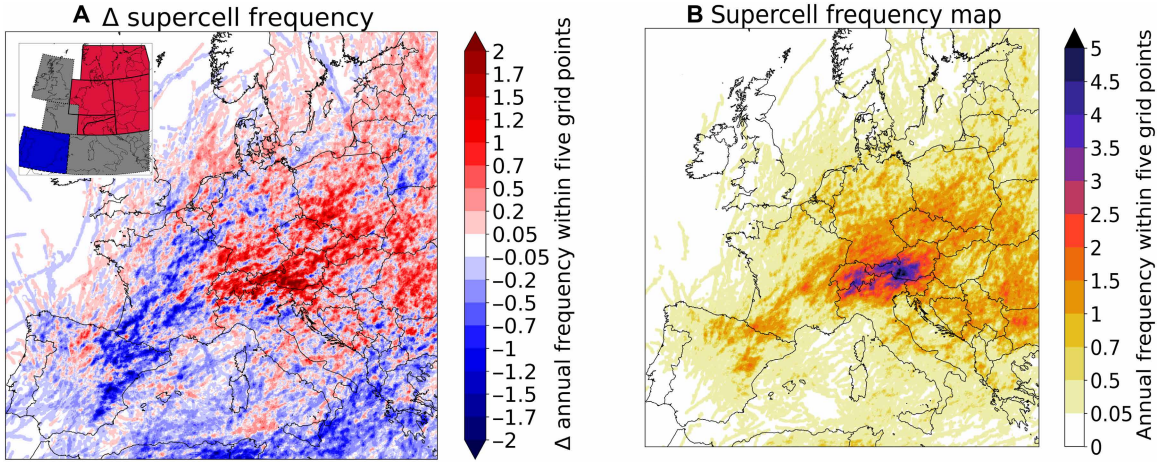

Fig. 3. Supercell tracks in future climate simulation showing an overall increase in occurrence frequency and a shift toward northeastern Europe and higher altitudes. (**A**) Annual average difference in supercell track frequency [future – present]; inset shows regionally aggregated significant changes in track number. Red, significant positive; blue, significant negative; gray, no significant change. (**B**) Annual average supercell track frequency at +3°C, within five grid points.

Table 1. Regional supercell changes showing significant changes in supercell frequency and their uncertainty. Regional annual supercell initiation frequency (*f*, year^{-1}), standard deviation (SD, year^{-1}), percentage of right-movers (% RM,%), and their bootstrapped mean relative change and 95% confidence interval (CI,%). Significant changes are marked in bold and with an asterisk (*).

Region	Current			Future			Relative change [%]	
	f	SD	% RM	*f*	SD	% RM	Δ *f* [95% CI]	Δ% RM [95% CI]
British Isles (BI)	4.5	4.3	86	5.5	1.9	82	32 [−25,130]	28 [−4, 88]
Eastern Europe (EE)	87	28.2	90	135	41.6	89	* **56 [42, 72]**	[−3, 1]
France (FR)	46	15.9	85	39	17.7	86	−15 [−30, 2]	1 [−5, 6]
Iberian Peninsula (IP)	115	23.1	81	84	24.4	80	* **−27 [−36, −28]**	[−6, 4]
Mediterranean (MD)	167	33.4	91	192	52.2	89	15 [2, 28]	* **−3 [−5, −1]**
Central Europe (CE)	61	31	91	81	30.1	89	* **36 [16, 61]**	−4 [−9, 1]
Baltic (BA)	10	6.1	98	21	8.3	92	* **116 [68, 187]**	* **−6 [−10, −3]**
Northern Alps (NAL)	38	26.2	89	57	27.4	87	* **52 [20, 90]**	−3 [−7, 0]
Southern Alps (SAL)	61	25.6	91	82	22.2	90	* **36 [21, 52]**	−3 [−7, 1]
Entire domain	714	115	88	794	123	87	* **11 [6, 16]**	−1 [−2, 0]

increases occur over eastern Europe, central Europe, and both Alpine areas, while the Iberian Peninsula experiences a significant decrease. The overall number of supercells increases by 11%. Right-moving storms prevail in all regions, making up ≥80% of all storms. Changes in future are small and largely statistically not significant(≤6%) but overall show a tendency for a slightly decreasing fraction of right movers.

Changes in convective environments

Figure 4 provides information on the changing convective environments between the two climate scenarios. Significance is tested per grid point on monthly aggregated values with a Wilcoxon-signed rank test at $P \leq 0.05$ and a false discovery rate correction (*55*, *56*). We investigate the frequency of convective available potential energy (CAPE) >100 J kg^{-1}, indicating the presence of instability. In the present climate, CAPE exhibits a meridional gradient, with greater values in southern regions and also over the sea (Fig. 4A), where moisture is readily available. It corresponds to the overall pattern of convective activity. The change in CAPE frequency is largely insignificant over land, with only the Alpine area and northeastern Europe experiencing significant increases, while the Iberian Peninsula and southeastern Europe experience significant decreases, matching the areas where supercell frequency decreases (Fig. 4C). The highest values of CAPE are found along mountain ranges, e.g., the southern fringes of the Alps, the Dinaric Alps, and the Pyrenees (Fig. 4D). At 3°C warming, averages are increasing significantly across wide areas of continental Europe, especially in Switzerland, Austria, and Germany, and in eastern Europe. No significant increases are found over the Iberian Peninsula (Fig. 4F). We next inspect convective inhibition (CIN), while CAPE exceeds >100 J kg^{-1}. In the present climate, CIN follows the meridional gradient of CAPE, with greater values surrounding the Mediterranean (Fig. 4G). On the one hand, this dampens CI, as more energy is required to overcome the inhibition. On the other hand, greater CIN will allow CAPE to reach greater values before CI sets in. CIN is smaller over mountain ranges, facilitating CI. In the mountains, orographic processes (such as orographic lifting) also support CI. In the +3°C climate, CIN increases the most over the Iberian Peninsula, France, and Italy, matching the change in supercell activity (Fig. 4I). Since supercell thunderstorms require deep wind shear, we also inspect the average 925- to 500-hPa bulk shear, when CAPE > 100 J kg^{-1}. Shear is masked where the 925-hPa level is under the surface. In the present climate, the highest shear values are located off the Iberian coast, neighboring its mountain ranges, and to the south of the Massif Central and the Alps (Fig. 4J). Orographic flow is known to enhance wind shear through channeling effects and prescribing the flow direction, enhancing directional shear (*14*, *16*, *18*, *38*). In a warmer climate, shear increases significantly over most of the land area (Fig. 4L).

These environmental parameters support the change in supercell frequency. Over the Iberian Peninsula, where supercell frequency decreases significantly, CAPE is less frequently present, and when it is, it shows no significant change in magnitude. CIN, however, increases significantly, further contributing to decreasing frequency. The Iberian Peninsula is subject to strong surface warming, while specific humidity shows very little change and relative humidity strongly decreases (*57*). This contributes to decreasing instability and increasing inhibition. In central Europe, where the largest absolute increase takes place, the frequency of CAPE is increasing in the Alps, and the magnitude of CAPE is increasing over a larger area. CIN increases only moderately. With increasing temperatures, the slope of the moist adiabat increases, enabling CAPE to reach higher values, even if relative humidity is stable (*58*). In central Europe, 2-m specific humidity increases, so that 2-m relative humidity only slightly decreases, leading to greater instability (*57*). The Baltic area, with the largest relative increase in supercells, has an increase in CAPE frequency and magnitude and no significant change in CIN. It also has increases in near-surface specific and relative humidity while still experiencing significant warming (*57*).

The changes in environmental parameters highlight a less convectively favorable environment over the Iberian Peninsula and more favorable environments in central and northeastern Europe. This agrees with expected changes in moist adiabatic lapse rates and instability, which show increased subsidence and pronounced drying in the Mediterranean that result in increasing stability, while instability increases in central and eastern Europe, owed to a higher moisture availability in higher temperatures (*59*, *60*).

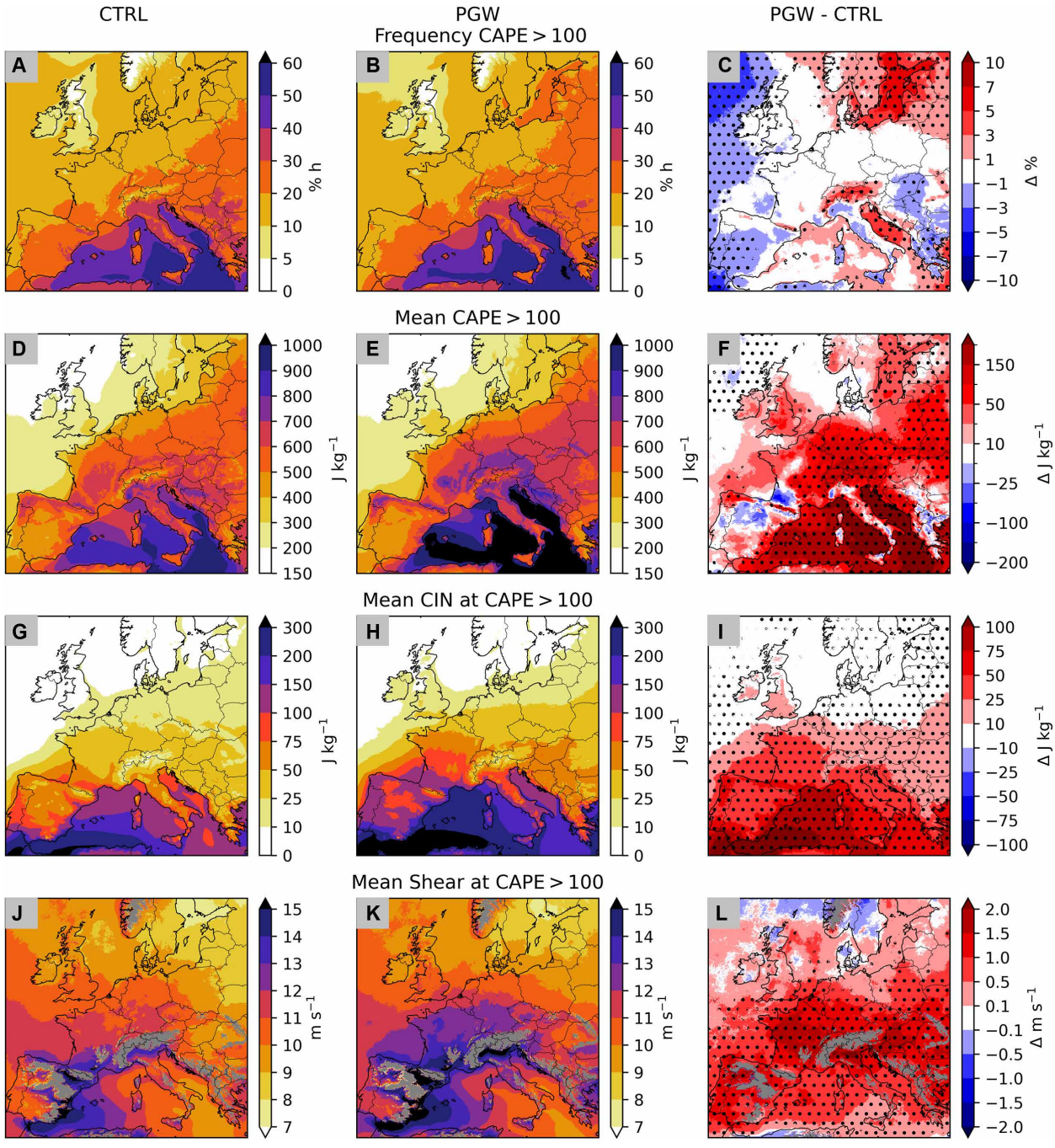

Fig. 4. Changes in convective environments align with changes in supercell frequency and intensity. Atmospheric environment in current (**A**, **D**, **G**, and **J**) and future climate (**B**, **E**, **H**, and **K**), and their difference (**C**, **F**, **I**, and **L**). Shown for the frequency of CAPE > 100 J kg^{-1} (% of hours, first row), mean CAPE > 100 J kg^{-1} (second row), mean CIN at CAPE > 100 J kg^{-1} (third row), and mean bulk shear at CAPE > 100 J kg^{-1} (last row). Significant changes are marked with dots.

Intensity changes

Figure 5 depicts supercell properties over the entire tracks for the whole domain in the current and future climate as empirical probability density functions. Each probability density function is normalized such that the total area equals 1, which means the density values scale inversely with the width of the *x*-axis range.

The overall track length and duration remain largely stable, indicating that the shifts in storm frequency are driven mostly by an increased number of storms, rather than longer tracks. Storm area, which is determined by the precipitation field, and peak precipitation rate increase in future, consistent with literature indicating an increase in subdaily, convective precipitation extremes in Europe (*23*, *57*), and supercell precipitation changes in the United States (*61*). The maximum hail size also increases (*57*). Peak wind gusts show only marginal increases (*62*). Peak updraft speeds and maximum vorticity also remain stable. While the overall supercell frequency

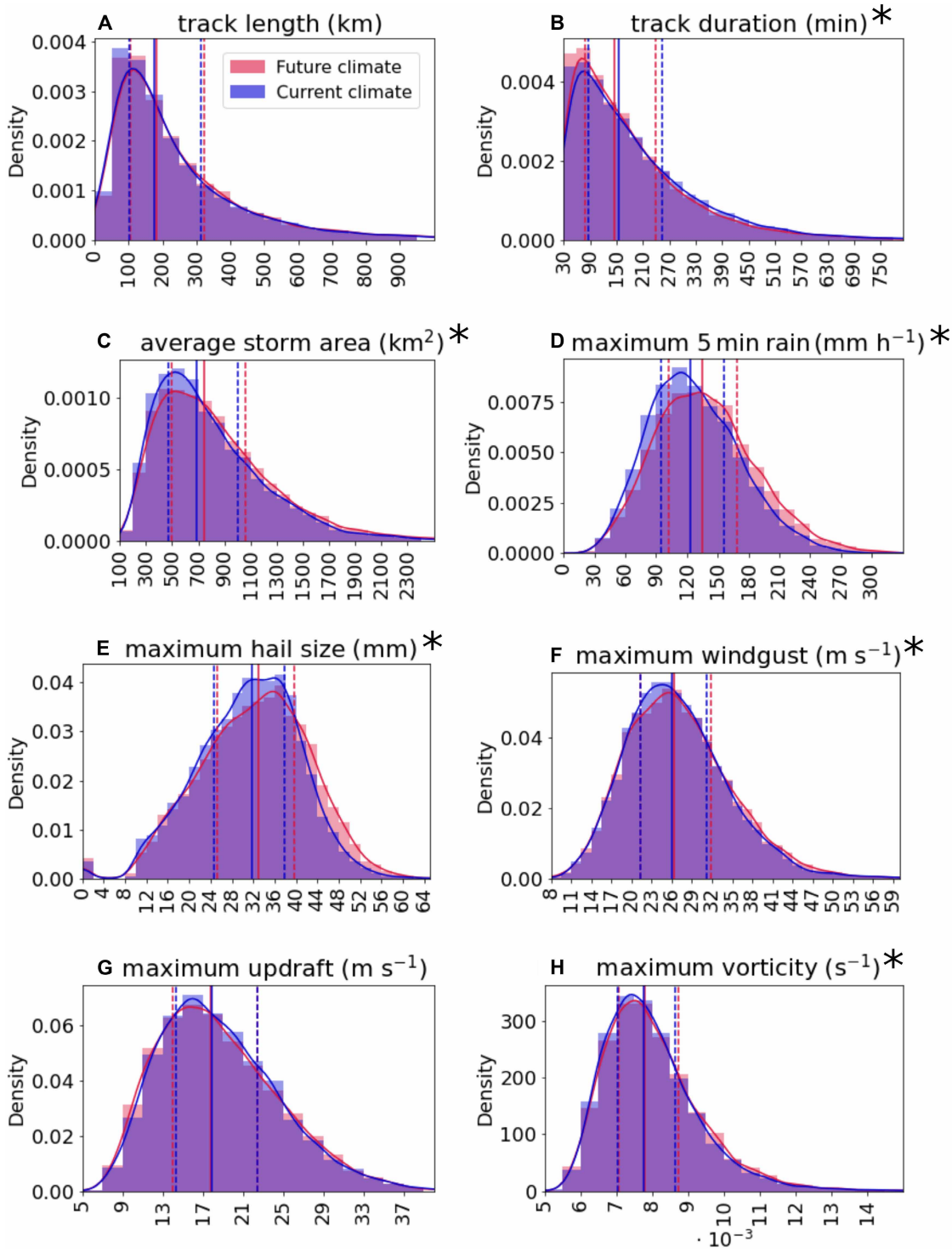

Fig. 5. Empirical probability density functions (integral of curve is always 1) of supercell track properties in both climate scenarios indicating an increase in precipitation-related intensity properties. The median is depicted with a solid line, the quartiles with dashed lines. Properties: (**A**) track length, (**B**) track duration, (**C**) average storm area, (**D**) peak precipitation rate, (**E**) maximum hail size, (**F**), maximum wind gust, (**G**) maximum updraft, and (**H**) maximum vorticity. Significant changes are marked with an asterisk (*).

increases and shifts toward the NE of Europe, most storm properties remain stable or increase in intensity. The intensity increase independent of regional frequency shift is also found for hailstorms in the same simulation setup (*63*). The most notable changes are an increase in precipitation (rain and hail) characteristics, which are significant under a Mann-Whitney-U test at the $P \leq 0.05$ level.

DISCUSSION

Severe convection in the European context

Given the sparsity of explicit pan-European supercell climatologies (as opposed to proxy analyses or hazard-oriented studies), we discuss the identified spatial distribution and trends. We discuss both past identified trends and modeled future trends, being aware that past trends do not automatically infer an identical future trend.

We first reflect on literature describing severe convection in the current climate over Europe. Overall, we find good agreement for the spatial pattern (*9*, *11*, *36*) and seasonal (*64*–*66*) and diurnal (*6*, *7*, *65*) cycles in the current climate scenario. Locally, differences can be found, such as the missing local hot spot in the Eastern Carpathian mountains (*8*), which may be due to unresolved local phenomena or observational artifacts.

The identification of a majority of right movers over vast areas of Europe is supported by a storm motion–based supercell classification in Germany, showing an observed right-mover majority (75%) (*39*). Kahraman *et al.* (*65*) identified a strong hailstorm hot spot in the fall in Greece based on hail proxies in kilometer-scale modeling. While the SE Mediterranean does experience increased supercell activity in the fall, there is no comparable hot spot. Europe-wide severe storm studies (*9*, *12*, *25*, *64*) generally agree with the more moderate activity in fall.

We next move to studies considering convective trends in Europe. The distribution shift of supercells toward the northeast in a warmer climate is in agreement with shifts in hail occurrence and extreme precipitation in the same simulation (*23*, *57*). Studies focusing on reconstructed trends by using observations to constrain a proxy show good agreement on the increase in activity in the past, particularly along the Alps (*66*–*68*). Studies investigating simulated future trends in extreme summer precipitation also show similar patterns in the Alpine area (*19*, *21*, *23*). Some future climate model, proxy-based studies disagree with the projected decrease in SW Europe (*69*, *70*); however, the proxies neither target supercells explicitly nor can they account for resolved storms. Rädler *et al.* (*70*) show agreement for shifts in lightning occurrence, but hailstorm proxies increase over the Iberian Peninsula. While Púčik *et al.* (*69*) do not find a decrease over southwestern Europe, they show no significant trends in this region. From an instability perspective, in future climate simulations, moist adiabatic lapse rates are expected to become less stable in northeastern Europe (*59*, *60*). This is consistent with the shift in supercell activity, CAPE frequency, and CAPE values. Overall, the literature provides good agreement for the tendency of supercells to occur more frequently in central and eastern Europe, less frequently in southwestern Europe, and increase strongly over the Alps.

Separated from frequency shifts, intensity in terms of rain rate, rain area, hail size, and wind gusts is significantly increasing (see fig. S1). This is in agreement with analyses of future climate studies of lightning and hailstorms in Europe, which find a general increase in hailstorm intensity independent of regional frequency changes, as the fraction of severe convective storms among all convective storms increases (*63*, *70*). Thermodynamic considerations on wind gusts also suggest an increasing intensity, confirmed by regional modeling experiments (*62*).

Table S3 provides an overview of the literature discussed here. We show here a pan-European supercell frequency map for the current climate and for a +3°C GWL. Now, supercells occur predominantly surrounding complex terrain, with the European hot spot lying in the Southern Alps. Prominent secondary areas lie around the Pyrenees and Spanish coast, over the Massif Central, along the Dinaric Alps, and over Southern Germany, which is in good agreement with current literature. Supercells occur predominantly in the afternoon, and activity peaks in summer, with the Mediterranean having a delayed peak in fall. In the future climate, the supercell frequency increases most over the Alpine hot spot, and the overall activity shifts toward the Northeast, with frequencies decreasing over France and Spain. Supercell properties see the biggest shift in storm area, precipitation intensity, and hail size, which significantly increase.

With >700 supercells per season in the current climate, they occur regularly throughout the continent but constitute an exceptional convective event in each location, ranging from <1 to >4 supercells per season. The significant 11% increase in overall supercell occurrence, and the increased intensity of precipitation hazards, stresses the importance of including supercell thunderstorms in weather risk assessments.

MATERIALS AND METHODS

European climate simulations

The simulations (*25*) are conducted with the COSMO graphics processing unit (GPU)-accelerated climate model (*71*–*73*). The horizontal grid spacing is ~2.2 km with a rotated latitude-longitude grid. This grid spacing is at the lower end of adequate resolution for supercell thunderstorms (*29*); however, all early idealized simulations of supercells also used a similar resolution (*74*, *75*). It also exceeds the 4-km grid spacing of similar work applied to the United States (*28*). The latter studies established the basic dynamical properties of supercell thunderstorms. In the vertical, there are 60 terrain-following, hybrid model levels; however, the output is stored on eight pressure levels. Both the hail growth model HAILCAST (*76*) and the lightning potential index (*77*, *78*) are implemented (*24*).

The modeling setup establishes a current and future climate scenario. For the current climate, 11 years of ERA-5 reanalysis data (2011–2021) (*30*) are used to enforce lateral and initial boundary conditions at a 3-hourly time step in a 12-km intermediate resolution domain with 3-hourly boundary updating, which drives a 2.2-km high-resolution domain with 1-hourly updating (*25*). The resulting, highly resolved output, provides data with a similar variability and occurrence of extreme events, as observed in this period (*27*). Precipitation, hail, and lightning data are stored at a 5-min time step, while the other surface and 3D variables are stored at an hourly interval. The future climate scenario uses the PGW approach (*79*, *80*), where a climate-change signal Δ is added to the boundary conditions of the reanalysis (*57*). We here use the PGW version introduced by Brogli *et al.* (*26*), which accounts for a mean annual cycle of thermodynamic, circulation, and sea surface temperature (SST) changes. To obtain the Δ, the Coupled Model Intercomparison Project Phase 6 (CMIP6) simulation of the GCM MPI-ESM1–2-HR (*81*, *82*) is used, selecting an ensemble member, particularly representative for summer

precipitation (*57*). The MPI-ESM1–2-HR is also one of the few models with the required spatio-temporal resolution in the output to obtain sufficiently dense data. It has also been shown to perform well for convective parameters in other regions (*83*). The Δ is computed using two 30-year time windows of the GCM simulation, one representing current conditions and the other representing future conditions at the time of the +3°C GWL. This forces a future climate simulation with a similar synoptic-scale event variability as the present, but in warmer climate conditions. In a recent investigation of the suitability of PGW (*84*), a detailed intercomparison between conventional and PGW downscaling was conducted, finding unexpectedly good performance of the PGW method for precipitation extremes, such as convective storms. The limitations of the setup used here and additional details on the PGW method are further discussed in (*57*), and more details on the current climate simulation are provided in (*25*).

Supercell tracking

To track supercell thunderstorms in a simulation with hourly pressure-level data, we have developed a classification method. First, convective cells are tracked using the 5-min precipitation field in a cell tracking algorithm [thresholds adapted from hailstorms to all thunderstorms from (*7*, *85*)]. A tracked cell has a minimum rain rate of 5.5 mm hour^{-1}, its peak must exceed 13.7 mm hour^{-1}, its area ≥ 10 grid points (~50 km^2), and its lifetime ≥ 30 min. To further classify the cells as supercells, the updraft and vertical vorticity are analyzed hourly at the 700-, 600-, 500-, and 400-hPa levels. A rotating updraft is defined by a minimum area of three grid points having $w \geq 5$ m s^{-1} and $\zeta \geq 5 \times 10^{-3}$ s^{-1}. This criterion must be fulfilled in at least two adjoining pressure levels. To allow for vertically tilting storms, each identified area is enlarged by a one grid point radius. Last, these identified areas must overlap with a tracked cell. To allow for sparsely precipitating updrafts, which may be displaced from the main precipitating area, rain cells are dilated with a one grid point radius. More details on the tracking methodology can be found in the "Supercell tracking" section in the Supplementary Materials.

Observational reference

To tune and validate the supercell tracking in the model data (see the "Case-based model validation" secition in Results), a 6-year supercell dataset from the Swiss radar domain is used (*32*). Radar-based mesocyclone tracking uses radar reflectivity to track thunderstorms and subsequently identifies vertically continuous rotation in the Doppler velocity field (*7*). Given the different nature of radar-based mesocyclone detection and supercell tracking in model data in a dynamically downscaled simulation, this serves as a qualitative comparison for days with supercellular activity in the Alpine region.

Supplementary Materials

This PDF file includes:

Supplementary Text
Figs. S1 to S7
Tables S1 to S3
References

REFERENCES AND NOTES

1. R. Davies-Jones, A review of supercell and tornado dynamics. *Atmos. Res.* **158-159**, 274–291 (2015).
2. S. Bowen, B. Kerschner, J. Zheng Ng, 2023 Natural Catastrophe and Climate Report (Gallagher Re, 2024); www.ajg.com/gallagherre/news-and-insights/2024/january/2023-natural-catastrophe-and-climate-report/.
3. P. Hoeppe, Trends in weather related disasters - consequences for insurers and society. *Weather Clim. Extrem.* **11**, 70–79 (2016).
4. N. Nouri, N. Devineni, V. Were, R. Khanbilvardi, Explaining the trends and variability in the United States tornado records using climate teleconnections and shifts in observational practices. *Sci. Rep.* **11**, 1741 (2021).
5. V. A. Gensini, H. E. Brooks, Spatial trends in United States tornado frequency. *npj Clim. Atmos. Sci.* **1**, 1–5 (2018).
6. K. Wapler, Mesocyclonic and non-mesocyclonic convective storms in Germany: Storm characteristics and life-cycle. *Atmos. Res.* **248**, 105186 (2021).
7. M. Feldmann, U. Germann, M. Gabella, A. Berne, A characterisation of Alpine mesocyclone occurrence. *Weather Clim. Dyn.* **2**, 1225–1244 (2021).
8. R. Kvak, L. Okon, V. Bližňák, L. Méri, M. Kašpar, Spatial distribution and precipitation intensity of supercells: Response to terrain asymmetry in the Western Carpathians, Central Europe. *Atmos. Res.* **292**, 106885 (2023).
9. M. Taszarek, J. Allen, T. Púčik, P. Groenemeijer, B. Czernecki, L. Kolendowicz, K. Lagouvardos, V. Kotroni, W. Schulz, A climatology of thunderstorms across Europe from a synthesis of multiple data sources. *J. Clim.* **32**, 1813–1837 (2019).
10. A. Manzato, S. Serafin, M. M. Miglietta, D. Kirshbaum, W. Schulz, A pan-Alpine climatology of lightning and convective initiation. *Mon. Weather Rev.* **150**, 2213–2230 (2022).
11. S.-E. Enno, J. Sugier, R. Alber, M. Seltzer, Lightning flash density in Europe based on 10 years of ATDnet data. *Atmos. Res.* **235**, 104769 (2020).
12. H. J. Punge, K. M. Bedka, M. Kunz, A. Reinbold, Hail frequency estimation across Europe based on a combination of overshooting top detections and the ERA-INTERIM reanalysis. *Atmos. Res.* **198**, 34–43 (2017).
13. A. F. Prein, G. J. Holland, Global estimates of damaging hail hazard. *Weather Clim. Extrem.* **22**, 10–23 (2018).
14. B. Katona, P. Markowski, C. Alexander, S. Benjamin, The influence of topography on convective storm environments in the Eastern United States as deduced from the HRRR. *Weather Forecast.* **31**, 1481–1490 (2016).
15. A. W. Lyza, K. R. Knupp, A background investigation of tornado activity across the Southern Cumberland Plateau Terrain system of Northeastern Alabama. *Mon. Weather Rev.* **146**, 4261–4278 (2018).
16. B. Katona, P. Markowski, Assessing the influence of complex terrain on severe convective environments in Northeastern Alabama. *Weather Forecast.* **36**, 1003–1029 (2021).
17. A. W. Lyza, M. D. Flournoy, The influence of cell mergers on supercell characteristics and tornado evolution on 27-28 April 2011. *Mon. Weather Rev.* **151**, 1551–1569 (2023).
18. M. Feldmann, R. Rotunno, U. Germann, A. Berne, Supercell thunderstorms in complex topography–how mountain valleys with lakes can increase occurrence frequency. *Mon. Weather Rev.* **152**, 471–489 (2024).
19. N. Ban, J. Schmidli, C. Schär, Heavy precipitation in a changing climate: Does short-term summer precipitation increase faster? *Geophys. Res. Lett.* **42**, 1165–1172 (2015).
20. M. F. Cardell, A. Amengual, R. Romero, C. Ramis, Future extremes of temperature and precipitation in Europe derived from a combination of dynamical and statistical approaches. *Int. J. Clim.* **40**, 4800–4827 (2020).
21. N. Ban, J. Rajczak, J. Schmidli, C. Schär, Analysis of Alpine precipitation extremes using generalized extreme value theory in convection-resolving climate simulations. *Clim. Dyn.* **55**, 61–75 (2020).
22. H. J. Fowler, H. Ali, R. P. Allan, N. Ban, R. Barbero, P. Berg, S. Blenkinsop, N. S. Cabi, S. Chan, M. Dale, R. J. H. Dunn, M. Ekström, J. P. Evans, G. Fosser, B. Golding, S. B. Guerreiro, G. C. Hegerl, A. Kahraman, E. J. Kendon, G. Lenderink, E. Lewis, X. Li, P. A. O'Gorman, H. G. Orr, K. L. Peat, A. F. Prein, D. Pritchard, C. Schär, A. Sharma, P. A. Stott, R. Villalobos-Herrera, G. Villarini, C. Wasko, M. F. Wehner, S. Westra, A. Whitford, Towards advancing scientific knowledge of climate change impacts on short-duration rainfall extremes. *Philos. Trans. R. Soc. A Math. Phys. Eng. Sci.* **379**, 20190542 (2021).
23. R. Estermann, J. Rajczak, P. Velasquez, R. Lorenz, C. Schär, Projections of heavy precipitation characteristics over the greater alpine region using a kilometer-scale climate model ensemble. *J. Geophys. Res. Atmos.* **130**, e2024JD040901 (2025).
24. R. Cui, N. Ban, M.-E. Demory, C. Schär, Exploring hail and lightning diagnostics over the Alpine-Adriatic region in a km-scale climate model. *Weather Clim. Dyn. Discuss.* **4**, 905–926 (2023).
25. R. Cui, I. Thurnherr, P. Velasquez, K. Brennan, M. Leclair, A. Mazzoleni, T. Schmid, H. Wernli, C. Schär, A European hail and lightning climatology from an 11-year kilometer-scale regional climate simulation. *J. Geophys. Res. Atmos.* **130**, e2024JD042828 (2025).
26. R. Brogli, C. Heim, J. Mensch, S. L. Sørland, C. Schär, The pseudo-global-warming (PGW) approach: methodology, software package PGW4ERA5 v1.1, validation, and sensitivity analyses. *Geosci. Model Dev.* **16**, 907–926 (2023).
27. C. Heim, D. Leutwyler, C. Schär, Application of the Pseudo-Global Warming Approach in a Kilometer-Resolution Climate Simulation of the Tropics. *J. Geophys. Res. Atmos.* **128**, e2022JD037958 (2023).
28. A. S. Walker, A. M. Haberlie, V. A. Gensini, The future of supercells in the United States. *Bull. Am. Meteorol. Soc.* **104**, E1–E21 (2023).

29. A. F. Prein, R. M. Rasmussen, D. Wang, S. E. Giangrande, Sensitivity of organized convective storms to model grid spacing in current and future climates. *Philos. Trans. R. Soc. A Math. Phys. Eng. Sci.* **379**, 20190546 (2021).
30. H. Hersbach, B. Bell, P. Berrisford, S. Hirahara, A. Horányi, J. Muñoz-Sabater, J. Nicolas, C. Peubey, R. Radu, D. Schepers, A. Simmons, C. Soci, S. Abdalla, X. Abellan, G. Balsamo, P. Bechtold, G. Biavati, J. Bidlot, M. Bonavita, G. De Chiara, P. Dahlgren, D. Dee, M. Diamantakis, R. Dragani, J. Flemming, R. Forbes, M. Fuentes, A. Geer, L. Haimberger, S. Healy, R. J. Hogan, E. Hólm, M. Janisková, S. Keeley, P. Laloyaux, P. Lopez, C. Lupu, G. Radnoti, P. de Rosnay, I. Rozum, F. Vamborg, S. Villaume, J.-N. Thépaut, The ERA5 global reanalysis. *Q. J. R. Meteorol. Soc.* **146**, 1999–2049 (2020).
31. T. T. Warner, R. A. Peterson, R. E. Treadon, A tutorial on lateral boundary conditions as a basic and potentially serious limitation to regional numerical weather prediction. *Bull. Am. Meteorol. Soc.* **78**, 2599–2617 (1997).
32. M. Feldmann, A. Hering, M. Gabella, A. Berne, Hailstorms and rainstorms versus supercells–a regional analysis of convective storm types in the Alpine region. *npj Clim. Atmos. Sci.* **6**, 1–11 (2023).
33. J. Kopp, K. Schröer, C. Schwierz, A. Hering, U. Germann, O. Martius, The summer 2021 Switzerland hailstorms: Weather situation, major impacts and unique observational data. *Weather* **78**, 184–191 (2023).
34. N. Dotzek, P. Groenemeijer, B. Feuerstein, A. M. Holzer, Overview of ESSL's severe convective storms research using the European Severe Weather Database ESWD. *Atmo. Res.* **93**, 575–586 (2009).
35. H. Brooks, P. Marsh, A. Kowaleski, P. Groenemeijer, T. Thompson, C. Schwartz, C. Shafer, A. Kolodziej, N. Dahl, D. Buckey, Evaluation of European Storm Forecast Experiment (ESTOFEX) forecasts. *Atmos. Res.* **100**, 538–546 (2011).
36. J. T. Allen, I. M. Giammanco, M. R. Kumjian, H. Jurgen Punge, Q. Zhang, P. Groenemeijer, M. Kunz, K. Ortega, Understanding hail in the Earth system. *Rev. Geophys.* **58**, e2019RG000665 (2020).
37. F. D. Martin, S. Davolio, M. M. Miglietta, V. Levizzani, A conceptual model for the development of tornadoes in the complex orography of the Po valley. *Mon. Weather Rev.* **152**, 1357–1377 (2024).
38. P. Scheffknecht, S. Serafin, V. Grubišić, A long-lived supercell over mountainous terrain. *Q. J. R. Meteorol. Soc.* **143**, 2973–2986 (2017).
39. M. Tonn, J. Wilhelm, M. Kunz, Evaluating Bunkers' storm motion of hail-producing supercells and their storm-relative helicity in Germany. *Meteorol. Z.* **32**, 229–243 (2023).
40. T. Rigo, O. Rodríguez, J. Bech, C. Farnell, An observational analysis of two companion supercell storms over complex terrain. *Atmos. Res.* **272**, 106149 (2022).
41. T. Rigo, N. Pineda, Inferring the severity of a multicell thunderstorm evolving to supercell, by means of radar and total lightning. *J. Sev. Storms Meteorol.* **11**, 1–27 (2016).
42. J. Mateo, D. Ballart, C. Brucet, M. Aran, J. Bech, A study of a heavy rainfall event and a tornado outbreak during the passage of a squall line over Catalonia. *Atmos. Res.* **93**, 131–146 (2009).
43. Y. Martín, M. Cívica, E. Pham, Constructing a supercell database in spain using publicly available two-dimensional radar images and citizen science. *Ann. Am. Assoc. Geogr.* **111**, 1346–1366 (2021).
44. L. Bagaglini, R. Ingrosso, M. M. Miglietta, Synoptic patterns and mesoscale precursors of Italian tornadoes. *Atmos. Res.* **253**, 105503 (2021).
45. A. Manzato, Hail in Northeast Italy: Climatology and bivariate analysis with the sounding-derived indices. *J. Appl. Meteorol. Climatol.* **51**, 449–467 (2012).
46. E. Flaounas, S. Raveh-Rubin, H. Wernli, P. Drobinski, S. Bastin, The dynamical structure of intense Mediterranean cyclones. *Clim. Dyn.* **44**, 2411–2427 (2015).
47. K. Wapler, P. James, Thunderstorm occurrence and characteristics in Central Europe under different synoptic conditions. *Atmos. Res.* **158-159**, 231–244 (2015).
48. A. M. Fischer, K. M. Strassmann, M. Croci-Maspoli, A. M. Hama, R. Knutti, S. Kotlarski, C. Schär, C. S. Poberaj, N. Ban, M. Bavay, U. Beyerle, D. N. Bresch, S. Brönnimann, P. Burlando, A. Casanueva, S. Fatichi, I. Feigenwinter, E. M. Fischer, M. Hirschi, M. A. Liniger, C. Marty, I. Medhaug, N. Peleg, M. Pickl, C. C. Raible, J. Rajczak, O. Rössler, S. C. Scherrer, C. Schwierz, S. I. Seneviratne, M. Skelton, S. L. Sørland, C. Spirig, F. Tschurr, J. Zeder, E. M. Zubler, Climate scenarios for Switzerland CH2018 - approach and implications. *Clim. Serv.* **26**, 100288 (2022).
49. P. M. Markowski, N. Dotzek, A numerical study of the effects of orography on supercells. *Atmos. Res.* **100**, 457–478 (2011).
50. S. Gnann, J. W. Baldwin, M. O. Cuthbert, T. Gleeson, W. Schwanghart, T. Wagener, The influence of topography on the global terrestrial water cycle. *Rev. Geophys.* **63**, e2023RG000810 (2025).
51. D. M. Schultz, M. V. Young, D. J. Kirshbaum, The Spanish plume elevated mixed layer: Review of its use and misuse within the scientific literature. *Mon. Weather Rev.* **153**, 737–761 (2025).
52. F. Li, D. R. Chavas, K. A. Reed, N. Rosenbloom, D. T. Dawson II, The role of elevated terrain and the gulf of Mexico in the production of severe local storm environments over North America. *J. Clim.* **34**, 7799–7819 (2021).
53. K. L. Rasmussen, R. A. Houze, Convective initiation near the andes in subtropical South America. *Mon. Weather Rev.* **144**, 2351–2374 (2016).
54. E. Flaounas, S. Davolio, S. Raveh-Rubin, F. Pantillon, M. M. Miglietta, M. A. Gaertner, M. Hatzaki, V. Homar, S. Khodayar, G. Korres, V. Kotroni, J. Kushta, M. Reale, D. Ricard, Mediterranean cyclones: Current knowledge and open questions on dynamics, prediction, climatology and impacts. *Weather Clim. Dyn.* **3**, 173–208 (2022).
55. V. Ventura, C. J. Paciorek, J. S. Risbey, Controlling the proportion of falsely rejected hypotheses when conducting multiple tests with climatological data. *J. Clim.* **17**, 4343–4356 (2004).
56. Y. Benjamini, Y. Hochberg, Controlling the false discovery rate: A practical and powerful approach to multiple testing. *J. R. Stat. Soc. Ser. B* **57**, 289–300 (1995).
57. I. Thurnherr, R. Cui, P. Velasquez, H. Wernli, C. Schär, The effect of 3°C global warming on hail over Europe. *Authorea*, 10.22541/au.173809555.59545480/v1 (2025).
58. K. Emanuel, On the physics of high CAPE. *J. Atmos. Sci.* **80**, 2669–2683 (2023).
59. R. Brogli, S. Lund Sørland, N. Kröner, C. Schär, Future summer warming pattern under climate change is affected by lapse-rate changes. *Weather Clim. Dyn.* **2**, 1093–1110 (2021).
60. R. Brogli, N. Kröner, S. L. Sørland, D. Lüthi, C. Schär, The role of hadley circulation and lapse-rate changes for the future European summer climate. *J. Clim.* **32**, 385–404 (2019).
61. A. W. Zeeb, W. S. Ashley, A. M. Haberlie, V. A. Gensini, A. C. Michaelis, Supercell precipitation contribution to the United States hydroclimate. *Int. J. Climatol.* **44**, 1489–1512 (2024).
62. A. F. Prein, Thunderstorm straight line winds intensify with climate change. *Nat. Clim. Chang.* **13**, 1353–1359 (2023).
63. K. P. Brennan, I. Thurnherr, M. Sprenger, H. Wernli, Insights from hailstorm track analysis in European climate change simulations. *EGUsphere*, 1–29 (2025).
64. M. Taszarek, J. T. Allen, P. Groenemeijer, R. Edwards, H. E. Brooks, V. Chmielewski, S.-E. Enno, Severe convective storms across Europe and the United States. Part I: Climatology of lightning, large hail, severe wind, and tornadoes. *J. Clim.* **33**, 10239–10261 (2020).
65. A. Kahraman, E. J. Kendon, H. J. Fowler, Climatology of severe hail potential in Europe based on a convection-permitting simulation. *Clim. Dyn.* **62**, 6625–6642 (2024).
66. J. Wilhelm, S. Mohr, H. J. Punge, B. Mühr, M. Schmidberger, J. E. Daniell, K. M. Bedka, M. Kunz, Severe thunderstorms with large hail across Germany in June 2019. *Weather* **76**, 228–237 (2021).
67. F. Battaglioli, P. Groenemeijer, T. Púčik, M. Taszarek, U. Ulbrich, H. Rust, Modeled multidecadal trends of lightning and (Very) large hail in Europe and North America (1950-2021). *J. Appl. Meteorol. Climatol.* **62**, 1627–1653 (2023).
68. M. Taszarek, J. T. Allen, H. E. Brooks, N. Pilguj, B. Czernecki, Differing trends in United States and European severe thunderstorm environments in a warming climate. *Bull. Am. Meteorol. Soc.* **102**, E296–E322 (2021).
69. T. Púčik, P. Groenemeijer, A. T. Rädler, L. Tijssen, G. Nikulin, A. F. Prein, E. van Meijgaard, R. Fealy, D. Jacob, C. Teichmann, Future changes in European severe convection environments in a regional climate model ensemble. *J. Clim.* **30**, 6771–6794 (2017).
70. A. T. Rädler, P. H. Groenemeijer, E. Faust, R. Sausen, T. Púčik, Frequency of severe thunderstorms across Europe expected to increase in the 21st century due to rising instability. *npj Clim. Atmos. Sci.* **2**, 1–5 (2019).
71. M. Baldauf, A. Seifert, J. Förstner, D. Majewski, M. Raschendorfer, T. Reinhardt, Operational convective-scale numerical weather prediction with the COSMO model: Description and sensitivities. *Mon. Weather Rev.* **139**, 3887–3905 (2011).
72. D. Leutwyler, O. Fuhrer, X. Lapillonne, D. Lüthi, C. Schär, Towards European-scale convection-resolving climate simulations with GPUs: A study with COSMO 4.19. *Geosci. Model Dev.* **9**, 3393–3412 (2016).
73. C. Schär, O. Fuhrer, A. Arteaga, N. Ban, C. Charpilloz, S. D. Girolamo, L. Hentgen, T. Hoefler, X. Lapillonne, D. Leutwyler, K. Osterried, D. Panosetti, S. Rüdisühli, L. Schlemmer, T. C. Schulthess, M. Sprenger, S. Ubbiali, H. Wernli, Kilometer-scale climate models: Prospects and challenges. *Bull. Am. Meteorol. Soc.* **101**, E567–E587 (2020).
74. M. L. Weisman, J. B. Klemp, The dependence of numerically simulated convective storms on vertical wind shear and buoyancy. *Mon. Weather Rev.* **110**, 504–520 (1982).
75. R. Rotunno, J. B. Klemp, M. L. Weisman, A theory for strong, long-lived squall lines. *J. Atmos. Sci.* **45**, 463–485 (1988).
76. R. D. Adams-Selin, C. L. Ziegler, Forecasting hail using a one-dimensional hail growth model within WRF. *Mon. Weather Rev.* **144**, 4919–4939 (2016).
77. Y. Yair, B. Lynn, C. Price, V. Kotroni, K. Lagouvardos, E. Morin, A. Mugnai, M. del Carmen Llasat, Predicting the potential for lightning activity in Mediterranean storms based on the Weather Research and Forecasting (WRF) model dynamic and microphysical fields. *J. Geophys. Res. Atmos.* **115**, D04205 (2010).
78. B. Lynn, Y. Yair, Prediction of lightning flash density with the WRF model. *Adv. Geosci.* **23**, 11–16 (2010).
79. T. Sato, F. Kimura, A. Kitoh, Projection of global warming onto regional precipitation over Mongolia using a regional climate model. *J. Hydrol.* **333**, 144–154 (2007).
80. C. Schär, C. Frei, D. Lüthi, H. C. Davies, Surrogate climate-change scenarios for regional climate models. *Geophys. Res. Lett.* **23**, 669–672 (1996).
81. J.-S. von Storch, D. Putrasahan, K. Lohmann, O. Gutjahr, J. Jungclaus, M. Bittner, H. Haak, K.-H. Wieners, M. Giorgetta, C. Reick, M. Esch, V. Gayler, P. de Vrese, T. Raddatz,

T. Mauritsen, J. Behrens, V. Brovkin, M. Claussen, T. Crueger, I. Fast, S. Fiedler, S. Hagemann, C. Hohenegger, T. Jahns, S. Kloster, S. Kinne, G. Lasslop, L. Kornblueh, J. Marotzke, D. Matei, K. Meraner, U. Mikolajewicz, K. Modali, W. Müller, J. Nabel, D. Notz, K. Peters-von Gehlen, R. Pincus, H. Pohlmann, J. Pongratz, S. Rast, H. Schmidt, R. Schnur, U. Schulzweida, K. Six, B. Stevens, A. Voigt, E. Roeckner, MPI-M MPIESM1.2-HR model output prepared for CMIP6 HighResMIP. *Earth Syst. Grid Fed.*, 10.22033/ESGF/CMIP6.762 (2017).

82. V. Eyring, S. Bony, G. A. Meehl, C. A. Senior, B. Stevens, R. J. Stouffer, K. E. Taylor, Overview of the Coupled Model Intercomparison Project Phase 6 (CMIP6) experimental design and organization. *Geosci. Model Dev.* **9**, 1937–1958 (2016).
83. D. R. Chavas, F. Li, Biases in CMIP6 historical U.S. severe convective storm environments driven by biases in mean-state near-surface moist static energy. *Geophysical Research Letters* **49**, e2022GL098527 (2022).
84. A. Hall, S. Rahimi, J. Norris, N. Ban, N. Siler, L. R. Leung, P. Ullrich, K. A. Reed, A. F. Prein, Y. Qian, An evaluation of dynamical downscaling methods used to project regional climate change. *J. Geophys. Res. Atmos.* **129**, e2023JD040591 (2024).
85. K. P. Brennan, M. Sprenger, A. Walser, M. Arpagaus, H. Wernli, An object-based and Lagrangian view on an intense hailstorm day in Switzerland as represented in COSMO-1E ensemble hindcast simulations. *EGUsphere*, 1–31 (2024).
86. M. Blanc, M. Feldmann, Supercell track model data from a current and a future climate European COSMO simulations (2024); https://zenodo.org/records/13378058.
87. KillianBrennan, KillianBrennan/cell_tracker: Cell tracker as used for analysis in the WCD case study paper (Zenodo, 2024); https://doi.org/10.5281/zenodo.12685276.
88. M. Blanc, mblanc-abm/SC_tracker: Supercell detection and tracking algorithm; data analysis code (Zenodo, 2024), https://doi.org/10.5281/zenodo.13960265.
89. B. Federer, A. Waldvogel, W. Schmid, H. H. Schiesser, F. Hampel, M. Schweingruber, W. Stahel, J. Bader, J. F. Mezeix, N. Doras, G. D'Aubigny, G. DerMegreditchian, D. Vento, Main results of grossversuch IV. *J. Appl. Meteorol. Climatol.* **25**, 917–957 (1986).
90. R. A. Houze, W. Schmid, R. G. Fovell, H.-H. Schiesser, Hailstorms in Switzerland: Left movers, right movers, and false hooks. *Mon. Weather Rev.* **121**, 3345–3370 (1993).
91. R. Kaltenboeck, M. Steinheimer, Radar-based severe storm climatology for Austrian complex orography related to vertical wind shear and atmospheric instability. *Atmos. Res.* **158-159**, 216–230 (2015).
92. T. Voormansik, T. Müürsepp, P. Post, Climatology of convective storms in Estonia from radar data and severe convective environments. *Remote Sens* **13**, 2178 (2021).
93. K. Wapler, The life-cycle of hailstorms: Lightning, radar reflectivity and rotation characteristics. *Atmos. Res.* **193**, 60–72 (2017).
94. K. Wapler, T. Hengstebeck, P. Groenemeijer, Mesocyclones in Central Europe as seen by radar. *Atmos. Res.* **168**, 112–120 (2016).
95. L. Blašković, D. Jelić, B. Malečić, B. Omazić, I. Güttler, M. Telišman Prtenjak, Trend analysis and climatology of hail in Croatia. *Atmos. Res.* **294**, 106927 (2023).

Acknowledgments: We thank R. Trapp for the advice and insightful discussions. The simulations were conducted with support from PRACE (Partnership for Advanced Computing in Europe) on Piz Daint at the Swiss National Supercomputing Centre (CSCS). **Funding:** We acknowledge the support of SNSF grant CRSII5_201792, funding the Synergia-project "Seamless coupling of kilometer-resolution weather predictions and climate simulations with hail impact assessments for multiple sectors" (scClim; https://scclim.ethz.ch/), which funded the work of I.T., K.P.B., and O.M. We furthermore acknowledge the support of the Mobiliar Insurance Group, funding the positions of M.F. and O.M. **Author contributions:** The project scope and outline was developed by M.F., O.M., and C.S. The tracking of supercell thunderstorms in the climate simulations was developed and conducted by M.B. as part of his Master thesis, under the supervision of M.F. and with the guidance of O.M. and C.S. M.F. analyzed the track data and prepared the visualizations. The thunderstorm cell tracking algorithm was developed by K.P.B. The climate simulations were performed by I.T. and P.V. The manuscript was written by M.F. and edited and revised by M.B., K.P.B., I.T., P.V., O.M., and C.S. **Competing interests:** M.F. and O.M. are in positions funded by the Mobiliar Insurance Group. This funding source played no role in any part of the study. The other authors declare that they have no competing interests. **Data and materials availability:** All data needed to evaluate the conclusions in the paper are present in the paper and/or the Supplementary Materials. The supercell track dataset is publicly available at zenodo.org (https://doi.org/10.5281/zenodo.13378058) (*86*). The thunderstorm tracking algorithm is documented in (*85*) and available at https://zenodo.org/records/12685276 (*87*). The supercell tracking algorithm and the analysis and visualization are available at https://doi.org/10.5281/zenodo.13960265 (*88*).

Submitted 26 February 2025
Accepted 29 July 2025
Published 27 August 2025
10.1126/sciadv.adx0513